

UC Berkeley

UC Berkeley Previously Published Works

Title

Harnessing Noncovalent Interactions in Dual-Catalytic Enantioselective Heck–Matsuda Arylation

Permalink

<https://escholarship.org/uc/item/35q612bg>

Journal

Journal of the American Chemical Society, 141(2)

ISSN

0002-7863

Authors

Reddi, Yernaïdu
Tsai, Cheng-Che
Avila, Carolina M
[et al.](#)

Publication Date

2019-01-16

DOI

10.1021/jacs.8b11062

Peer reviewed



Published in final edited form as:

J Am Chem Soc. 2019 January 16; 141(2): 998–1009. doi:10.1021/jacs.8b11062.

Harnessing Noncovalent Interactions in Dual-Catalytic Enantioselective Heck–Matsuda Arylation

Yernaïdu Reddi[†], Cheng-Che Tsai[‡], Carolina M. Avila[‡], F. Dean Toste^{*,‡}, and Raghavan B. Sunoj^{*,†}

[†]Department of Chemistry, Indian Institute of Technology Bombay, Powai, Mumbai 400076, India

[‡]Department of Chemistry, University of California Berkeley, Berkeley, California 94720, United States

Abstract

The use of more than one catalyst in one-pot reaction conditions has become a rapidly evolving protocol in the development of asymmetric catalysis. The lack of molecular insights on the mechanism and enantioselectivity in dual-catalytic reactions motivated the present study focusing on an important catalytic asymmetric Heck–Matsuda cross-coupling. A comprehensive density functional theory (M06 and B3LYP-D3) investigation of the coupling between a spirocyclic cyclopentene and 4-fluorophenyl diazonium species under a dual-catalytic condition involving Pd₂(dba)₃ (dba = *trans,trans*-dibenzylideneacetone) and chiral 2,2′-binaphthyl diamine (BINAM)-derived phosphoric acids (BDPA, 2,2′-binaphthyl diamine-derived phosphoric acids) is presented. Among various mechanistic possibilities examined, the pathway with explicit inclusion of the base (in situ generated sodium bicarbonate/sodium biphosphate) is found to be energetically more preferred over the analogous base-free routes. The chiral phosphate generated by the action of sodium carbonate on BDPA is found to remain associated with the reaction site as a counterion. The initial oxidative addition of Pd(0) to the aryl diazonium bond gives rise to a Pd-aryl intermediate, which then goes through the enantiocontrolling migratory insertion to the cyclic alkene, leading to an arylated cycloalkene intermediate. Insights on how a series of noncovalent interactions, such as C–H...O, C–H...N, C–H...F, C–H... π , Ip... π , O–H... π , and C–F... π , in the enantiocontrolling transition state (TS) render the migration of the Pd-aryl to the *si* prochiral face of the cyclic alkene more preferred over that to the *re* face are utilized for modulating the enantioselectivity. Aided by molecular insights on the enantiocontrolling transition states, we predicted improved enantioselectivity from 37% to 89% by changes in the N-aryl substituents of the catalyst. Subsequent experiments in our laboratory offered very good agreement with the predicted enantioselectivities.

*Corresponding Authors fdtoste@berkeley.edu, sunoj@chem.iitb.ac.in.

ASSOCIATED CONTENT

Supporting Information

The Supporting Information is available free of charge on the ACS Publications website at DOI: 10.1021/jacs.8b11062.

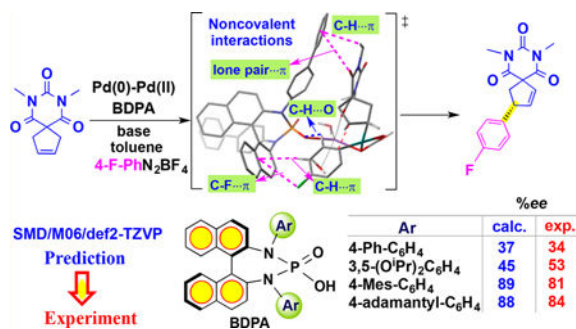
Optimized geometries, higher-energy alternative pathways, and Cartesian coordinates of all stationary points (PDF)

Experimental procedure, spectral details, and HPLC profile (PDF)

Notes

The authors declare no competing financial interest.

Graphical Abstract



INTRODUCTION

The most recent practices in asymmetric catalysis make use of different types of catalysts in one-pot conditions. The catalytic ability of more than one well-established catalyst is combined in such multicatalytic reactions. A gamut of dual-catalytic protocols employing two organocatalysts, two transition-metal catalysts, and a combination of organo- and transition-metal catalysts have found interesting applications in stereoselective synthesis of natural and biologically active products.¹ Among the various catalytic reactions involving single catalyst, transition-metal-catalyzed cross-coupling reactions constitute an important class, particularly for asymmetric synthesis of complex targets.² A valuable variant of the conventional coupling reaction is Heck–Matsuda reaction, wherein an aryl group, in the form of a diazonium salt, is coupled with an alkene using Pd catalysis.³ Heck–Matsuda arylation is a useful synthetic protocol for the construction of C–C bonds because of the ready availability of aryl diazonium salts, which are thermally stable and safer to work with.⁴ While Heck–Matsuda cross-coupling strategy is widely found in literature, the corresponding asymmetric versions remain much less reported, perhaps due to the compatibility issues between the commonly used chiral phosphine ligands and diazonium salts.⁵ In the past decade, Heck–Matsuda arylation has also been employed as a key step in the asymmetric synthesis of biologically active compounds.⁴ Excellent methods to overcome such issues were in arylative desymmetrization of cyclic and acyclic alkenes by using chiral bisoxazoline ligands.⁶ Highly enantio- and regioselective arylations of alkenyl alcohols using chiral pyridine oxazoline ligands reported by the Sigman group serve as a convincing demonstration of the potential of Heck–Matsuda cross-coupling.⁷

In recent years, chiral ion-pairing catalysts have been utilized under phase-transfer conditions. Enantioselective reactions proceeding through a cationic intermediate that can form an ion pair with an enantiomerically pure chiral anion of the catalyst are generally termed asymmetric counteranion-directed catalysis (ACDC).⁸ The idea of engaging 1,1'-bi-2-naphthol (BINOL)-derived chiral phosphoric acids as a chiral anion phase-transfer organocatalyst in conjunction with other transition-metal catalysts is particularly noteworthy.⁹ The use of chiral 2,2'-binaphthyl diamine (BINAM)-derived phosphoric acid catalysts in asymmetric reactions has been reported by the groups of Terada, Ishihara, and Toste.¹⁰ We have recently demonstrated an enantioselective Heck–Matsuda coupling using a combination of BINAM-derived phosphoric acids (BDPAs) and a Pd catalyst.¹¹

In one such interesting example, a spirocyclic cyclopentene derivative (**A1**) was reacted with 4-fluorophenyldiazonium tetrafluoroborate (**D1**) using Pd₂(dba)₃ and various BDPAs as the catalysts to the desired coupled product (**P1**) in high yield and enantioselectivities (Scheme 1).¹¹ The use of a base (such as Na₂CO₃ and Na₂HPO₄) was found to be necessary for improved yields and enantioselectivity (vide infra, Table 2). The representative example shown here is intended to convey two of our key motivations behind this study. First, the given catalyst–substrate combination **C1–A1–D1** constitutes the actual starting point of our computational study where the objective was to identify the potential reasons for poor enantioselectivity. Next, we wanted to examine whether knowledge of the enantiocontrolling transition states might help predict modifications toward improved stereoinduction, thereby setting a broader goal of computationally aided experiments in asymmetric catalysis.

Although there have been reports toward addressing mechanistic and selectivity issues in Heck-type as well as Heck–Matsuda desymmetrization reactions,¹² mechanism and origin of enantioselectivity on Heck–Matsuda arylation under dual-catalytic conditions have not been reported. In particular, the effect of the N-aryl substituents on BDPA catalysts on enantioselectivity is of timely importance for Heck–Matsuda arylations and other related reactions. Similarly, insights on the role of base as an active ingredient in the catalytic cycle demand attention. The question of whether the base participates only in one step of the reaction prior to, or during, the catalytic cycle remains unclear. In view of this, we have undertaken a detailed density functional theory investigation to gain mechanistic insights as well as to identify the factors responsible for enantiocontrol in the asymmetric Heck–Matsuda arylation of spirocyclic cyclopentene and cycloheptene derivatives with various aryl diazonium salts as substrates under a dual-catalytic condition provided by BDPAs and Pd₂(dba)₃. As a demonstration of the proof of concept that computational insights could be applied to the development of dual-catalytic reaction, additional efforts were also expended by way of new experiments to validate the predicted enantioselectivities on a few representative catalysts and substrate.

RESULTS AND DISCUSSION

This section is organized into three major subsections. First, the most important elementary steps in the mechanism of asymmetric Heck–Matsuda coupling, as obtained through our computational investigation, are provided. A comprehensive description of the molecular origin of enantioselectivity for a representative catalyst and substrates combination is then presented. Emphasis is placed on how the molecular insights could be exploited toward modulating the enantioselectivity induced by the chiral catalyst. In the last subsection, details of experimental validation of the computed enantioselectivities are summarized.

Mechanistic Details of Heck–Matsuda Arylation.

To begin with, the reaction between 4-fluorophenyl diazonium salt (**D1**) and spirocyclic cyclopentene (**A1**) in the presence of Na₂CO₃ under a dual-catalytic condition involving Pd₂(dba)₃ and BDPA–**C1** catalyst is examined (Scheme 2). The idea has been to learn from an example that yields poor enantioselectivity, which oftentimes is a common scenario during the developmental phase of a new asymmetric transformation. The deprotonation of

phosphoric acid **C1** by Na_2CO_3 can give a sodium salt of chiral phosphate and NaHCO_3 . In the next step, the substrate diazonium salt can interact with the sodium phosphate to form an ion-pair intermediate **1'**. On the basis of potential ligand variations around the palladium (native dba, in situ generated chiral phosphate, and NaHCO_3) and its mode of binding, four mechanistic possibilities are considered.¹³ We have also probed whether explicit inclusion of NaHCO_3 is desirable toward identifying the preferred mechanistic pathway. The mechanistic model consisting of NaHCO_3 along with the Pd catalyst and chiral phosphate is found to be energetically the most likely pathway compared to other alternatives devoid of NaHCO_3 (Scheme 2).¹³ The predicted energetic advantage is indeed borne out by additional experiments in the absence of any added base, which resulted in a dwindling yield of just 7% as opposed to 90% in the presence of Na_2CO_3 . This observation is also consistent with the computed energetic span (one of the energetic measures of the catalytic efficiency, vide infra), which is found to be 9.5 kcal/mol lower in the case of the NaHCO_3 -bound pathway than in its absence (counterion pathway, path D).¹⁴ Hence, we present the details of the NaHCO_3 -bound pathway here while other alternative routes are provided in the Supporting Information.¹³

The Gibbs free energy profile for the catalytic cycle is shown in Figure 1. The initial oxidative addition of the catalyst Pd(0) to the aryl-diazo bond leading to nitrogen extrusion exhibits a barrier of 14.3 kcal/mol (**TS(1–2)**). The geometric details for this step are provided in the Supporting Information (Figure S2). In this pathway, the bicarbonate is the primary ligand on palladium while the chiral phosphate interacts with the sodium ion in a κ^2 fashion. The uptake of the spirocyclic alkene (**A1**) by the palladated arene intermediate **2** in the subsequent step can lead to another catalyst–substrate intermediate **2'**. We have explicitly considered the participation of NaHCO_3 in the transition states (TSs) by maintaining a pentacoordinate environment around the sodium ion.¹⁵ In the next step, a migratory insertion of the spirocyclic cyclopentene leads to its arylation wherein the Pd-aryl group migrates to one of the alkenic carbon. This is the most important step that controls the enantioselectivity of the reaction. The barrier for the migratory insertion via **TS(2'–3)** is ~10 kcal/mol. The intrinsic reaction coordinate (IRC) calculations on **TS(2'–3)** reveal a concerted migratory insertion wherein the Pd–C_{aryl} bond breaking occurs simultaneously with the formation of Pd–C1 and C2–C_{aryl} bonds.¹⁶ The ensuing β -hydride elimination in intermediate **3** affords the desired product and a Pd–H species **4**.¹⁷ In the catalyst-regeneration step via a reductive elimination, the chiral phosphate can abstract a proton from **4** to give a Pd(0) species and chiral phosphoric acid.

Molecular Origin of the Enantiocontrolling Factors.

Because the migratory insertion step via **TS(2'–3)** is critical to the enantioselectivity, we have considered a total of 16 likely conformers as well as configurations for this TS. These comprise (i) conformers arising due to the rotation of the N-aryl group on the catalyst and (ii) configurations due to the differences in the positioning of the sodium phosphate around the palladium center.¹⁸ Because the experiments were conducted in both toluene and a 1:1 toluene–MTBE mixed solvent, we have evaluated the energetics in the continuum dielectric of pure toluene ($\epsilon = 2.38$) and an approximate one for the mixed solvent ($\epsilon = 3.44$). After a detailed sampling of various possibilities, the TS for the migration of the aryl group to the *si*

prochiral face of the spirocyclic alkene (**TS-si_{C1}**), leading to the *R* product, is found to be more favored than that to the *re* face (**TS-re_{C1}**). The differences in Gibbs free energies of the lower-energy diastereomeric TSs (**TS-si_{C1}** and **TS-re_{C1}**) are found to be 0.2 and 0.5 kcal/mol, respectively, in toluene (**M2**) and mixed-solvent (**M1**) conditions. Such small energy differences correspond to 17% and 39% enantiomeric excess (ee), respectively, in favor of the *R* enantiomer of the product. It should be acknowledged that we are comparing transition states that differ primarily in the stereochemical mode of approach in the bond formation, while the rest of the features remain nearly the same. The key to successful estimation of the very low energy difference between such transition states naturally demands rigorous consideration of various mechanistic pathways, configurational differences at the metal center, and careful sampling of the conformational space in each such situation.

After having noted the energetic advantage toward the formation of the *R* enantiomer of the arylated cycloalkene, we probed the stereoelectronic origin of the enantioselectivity by analyzing the geometries of the lower-energy diastereomeric TSs (Figure 2). Using the atoms in molecule (AIM) topological analysis of the electron-density distribution in the enantiocontrolling TSs, different types of weak noncovalent interactions (C–H...O, C–H... π , lone pair (lp)... π , O–H... π , and C–F... π)¹⁹ between the substrate (**A1** and **D1**) and the catalyst are identified. Only the C–H...O interaction (shown as *d* in Figure 2) between the substrate and the phosphate oxygen is found to be a common interaction present in both **TS-si_{C1}** and **TS-re_{C1}**. The C–H...O interaction is slightly better in the higher-energy **TS-re_{C1}** (2.24 Å) than in **TS-si_{C1}** (2.38 Å). Other weak interactions are unique to a given TS. For instance, another type of C–H...O interaction (*e*) between the cyclopentene C–H and the oxygen of the sodium-bound water (2.59 Å) is present in **TS-si_{C1}** but not in **TS-re_{C1}**. Similarly, C–H...O interaction (*j*) between the alkenyl C–H and the phosphate oxygen of the catalyst in **TS-re_{C1}** (2.40 Å) is absent in **TS-si_{C1}**. Overall, multiple C–H...O interactions seem to provide additional stabilization to **TS-re_{C1}** over that to **TS-si_{C1}**.

Another important and abundant noncovalent interaction noted in the migratory insertion TS is C–H... π (*a*, *e*, *h*, and *i* with a contact distance in the range of 2.58–3.13 Å). Among these, *h* and *i* are the catalyst–substrate interactions involving the π face of the N-aryl substituent of the catalyst and the alkene and/or aryl C–H bonds, respectively, of cyclopentene and fluoroarene. The fluoroaryl C–H interacts with the N-aryl substituent of the catalyst in **TS-re_{C1}** (denoted as *i*), but such an interaction is absent in **TS-si_{C1}** (Figure 2). A weak C–H... π interaction between the N-aryl substituent of the catalyst and the cyclopentene C–H (*a*) is noted in the lower-energy **TS-si_{C1}** but not in **TS-re_{C1}**. Another C–H... π interaction, between the binaphthyl backbone of the catalyst and the fluoroaryl C–H (*e*), is noted in **TS-si_{C1}**, whereas it is absent in **TS-re_{C1}**. Hence, the overall contribution of the C–H... π interactions is found to be more in **TS-si_{C1}** than in **TS-re_{C1}**. Other weak interactions, such as the lone pair... π (*b*) and C–F... π (*f*) are found only in the lower-energy **TS-si_{C1}**. The difference in relative strengths (as approximately gauged by the electron densities at the bond critical points along the bond paths) of these weak noncovalent interactions is found to be just marginal between these TSs.

In addition to the minor differences in the above-mentioned noncovalent interactions, two torsional angles of the N-aryl rings (*a*) and (*a'*) are identified as important (Figure 2).

Depending on how the substrates are positioned near the chiral phosphate and which one of the prochiral faces of the cycloalkene is involved in the migratory insertion, these torsional angles in **TS-si_{C1}** (37° and 0°) and **TS-re_{C1}** (43° and -37°) are found to be different. A comparison of the α and α' values as noted in the diastereomeric TSs and that in the native catalyst ($\alpha = 42^\circ$, $\alpha' = -35^\circ$) reveals that the α values of both the TSs are similar to that in the native catalyst. However, α' conveys a larger distortion in the lower-energy **TS-si_{C1}** than in **TS-re_{C1}** as compared to that in the native catalyst. Interestingly, a recent report by Milo et al. highlighted the importance of the torsion angle of the 3,3'-substituents in chiral BINOL-phosphate-catalyzed enantioselective reactions.²⁰ The torsion angle α' should be considered as an important distortion parameter playing a role in rendering the **TS-si_{C1}** as the more preferred TS. Another geometric feature of significance is the one involving the reaction coordinate, denoted as ϕ (C_{aryl}-Pd-C1-C2) and found to be -18.8° and 12.3°, respectively, in **TS-si_{C1}** and **TS-re_{C1}**. The distortion is expected to be lower when ϕ is closer to 0° for a square-planar geometry.

Besides the above-mentioned important localized distortions, the TSs could exhibit distortions elsewhere in the geometry. To capture such distortions (E_{dist}^\ddagger) as well as to analyze the role of interaction (E_{int}^\ddagger) between distorted reactants/catalyst in the TS, we have carried out activation-strain analysis (Table 1).²¹ In the activation-strain analysis of the TS, we have estimated the distortion energy within the reacting partners (i.e., spirocyclic cyclopentene/Pd-aryl moiety and chiral sodium phosphate) and the interaction energy between them (Table 1).²² The stabilizing interaction energy in **TS-si_{C1}** is found to be 10.2 kcal/mol more than that in **TS-re_{C1}** (Table 1). However, 6.7 kcal/mol higher distortion is noted in **TS-si_{C1}** as compared to that in **TS-re_{C1}**. Therefore, it is the more favorable interaction energy that makes **TS-si_{C1}** the lower-energy TS. This additional insight is in line with the geometric analysis using the relative distortions (ϕ , α , and α') in the diastereomeric TSs described in the previous paragraph.

Effect of N-aryl Substituents of BDPA Catalysts on the Enantioselectivity.

Thus far, two vital factors such as noncovalent interactions between the catalyst and substrates and distortion in both substrates and the catalyst are identified to correlate with the relative stabilization of the migratory insertion TSs. We wondered whether modulation of these factors, by way of changing the N-aryl substituents of the BINAM catalyst, might help improve the enantioselectivity. Additional computations on the entiocontrolling migratory insertion TSs are carried out with a different set of catalysts and substrates, as shown in Figure 3. In particular, enantioselectivities (ee's) are predicted using modified catalysts such as **C2**, **C3**, and **C4** for the same pair of substrates (A1 and D1).²³ The geometries of the lower-energy entiocontrolling TSs for the migration of the aryl group to the *si* and *re* face of the substrate as well as a summary of important noncovalent interactions are provided in Figures 4 and 5.

Careful comparison of the noncovalent interactions in the case of catalysts **C1** and **C3** revealed that a number of such interactions (*c*, *d*, *e*, *f*, and *h*) are common in both lower-energy TSs. Interestingly, more noncovalent interactions are identified in **TS-si_{C3}** than in **TS-si_{C1}**, whereas the corresponding higher-energy TS for the *re* face migration has nearly

equal number interactions for both **C1** and **C3** catalysts (Figure 4). Among the distortion parameters, the α values remained similar while α' showed a larger deviation upon changing the catalyst from **C1** to **C3**. These geometric deviations are evidently due to the change in the N-aryl substituents. Therefore, it appears that noncovalent interactions are more likely to impact the enantioselectivity in the case of catalyst **C3** as compared to **C1**.

The optimized TS geometries with catalyst **C1** and **A1–D1** as the coupling partners (Figure 2) indicate the presence of important noncovalent interactions involving the *para*-phenyl group of the N-aryl substituent of the catalyst. Hence, it will be intriguing to examine how substituents at the fourth position might influence the enantioselectivity. Following this lead, the enantiocontrolling TSs for different catalysts with varying N-aryl substituents, as shown in Figure 3, are identified for the coupling reaction between cycloalkenes such as **A1** and **A2** with diazonium salts **D1** and **D2**.

The detailed mapping of the noncovalent interactions in the enantiocontrolling TSs, as provided in Figure 4, suggests that the pattern of interactions changes as the N-aryl group on the catalyst is changed. The variations in the number and efficiency of such interactions lead to a difference in energy between **TS-*si*** and **TS-*re*** and, hence, the enantioselectivity. For instance, with **C1** as the catalyst and **A1–D1** as the coupling partners, two types of noncovalent interactions ($C-H \cdots \pi$ and $lp \cdots \pi$, respectively, denoted as *a* and *b* in Figure 2) are noticed in the lowest-energy migratory insertion TS, **TS-*si*_{C1}**. Interestingly, when the 4-aryl substituent of the N-aryl group is changed to a mesityl (**C2**) or an admantyl (**C3**) group, more effective noncovalent interactions (*a* and *b* for **TS-*si*_{C2}** and *m*, *l*, and *k* for **TS-*si*_{C3}**, as shown in Figure 4) between the catalyst and the substrate begin to appear. In the case of **C3** catalyst, both the number and strength of interactions are found to be higher in the lower-energy **TS-*si*_{C3}** than in **TS-*re*_{C3}**.

A graphical summary of noncovalent interactions in the migratory insertion TSs for catalysts **C1–C4** is provided in Figure 5. It can be noticed, in general, that there are more noncovalent interactions in the lower-energy **TS-*si*** as compared to that in **TS-*re*** (Figure 5a). Although quantitative estimates on several such intramolecular interactions in a TS are harder to evaluate, an approximate method could be to use the electron densities at the bond critical points (ρ_{bc_p}) between the interacting atoms, as obtained through the AIM calculations. Furthermore, counting the total number of noncovalent interactions as the sole matrix of overall favorable interaction in a TS may not be adequate, as lower numbers of stronger interactions can offset the effect of higher numbers of weaker interactions. However, for a given type of interaction, it is good to regard a larger value of ρ_{bc_p} as a relatively stronger interaction compared to a smaller value. We have tried to quantify the noncovalent interactions by using the Espinosa equation that makes use of the topological attributes such as ρ_{bc_p} , Laplacian electron density, and kinetic energy obtained through the AIM calculations.²⁴ Total number of noncovalent interactions, as identified through the bond paths and the corresponding interaction energies, are provided right above the bar diagram in Figure 5b. The total strength of noncovalent interactions in all the TSs for the *si*-face migration is more than that in the *re*-face, suggesting that such interactions do play a role in rendering the *si*-face migration relatively more favored.

Experimental Validation of the Predicted Enantioselectivities.

A number of experiments were carried out with a set of cycloalkenes, aryl diazonium, and modified BDPAs as shown in Figure 3.²⁵ A comparison of the predicted enantioselectivities and that obtained through experiments is summarized in Table 2.

On the basis of the insights gained through the analysis of the noncovalent interactions between the N-aryl substituents of catalyst **C1** with **D1** and **A1** as the substrates, we have examined the enantiocontrolling TSs for different cycloalkenes as well as N-aryl BDPAs. A summary of comparison of the predicted enantioselectivities to the corresponding experimental values is provided in Table 2. Some of the key highlights are that the lower enantioselectivities with cycloheptene when **C1**, **C2**, and **C3** are used as the catalyst could be improved by using diisopropoxy substituents as in catalyst **C4**.²⁶ This is a significant improvement in ee from 9% with C1 to 78% with C4.^{25,26} Careful analysis of the lower-energy diastereomeric TSs with these catalysts that determines the enantioselectivity helped us decipher important correlations. The total strength of the important noncovalent interactions in the lowest-energy diastereomeric TS for the migratory insertion to the *si* prochiral face of the alkene showed a steady increase upon going from catalyst **C1** to **C4**.²⁷ Thus, noncovalent interactions between the substrate and the catalyst as well as the distortions in them can be harnessed toward improving the enantioselectivity from 2% with catalyst **C1** to 86% with **C4**.²⁷

Another mechanistically relevant aspect is the role of base in the enantiocontrolling step of the reaction. We have located the migratory insertion TSs by using **C3** as a representative catalyst, in the presence of NaH₂PO₄ instead of NaHCO₃.²⁸ The TS geometries are found to be very similar to both NaHCO₃ and NaH₂PO₄. The predicted enantioselectivity with an explicitly included NaH₂PO₄ is found to be nearly the same as that obtained in the presence of NaHCO₃. Both predictions were verified through additional experiments, and it was found that they are in excellent agreement (Table 2). A comparison of the space-filling representation of these TSs revealed that the positioning of the dihydrogen phosphate or bicarbonate is somewhat away from the region of migratory insertion (Figure 6). It is therefore expected that a change of base from NaHCO₃ to NaH₂PO₄ is unlikely to impact the enantioselectivity.

Further, experiments are carried out with other bases such as Cs₂CO₃, ^tBuONa, and NaHCO₃ by using C1 catalyst to examine their potential impact on the yield and ee.²⁵ In line with the proposed involvement of the base in the precatalytic and catalytic steps as described in Scheme 2, we anticipated that the nature of the base could have a different effect on the reaction. Interestingly, the use of ^tBuONa as the base failed to yield any product. The % ee's obtained using C1 catalyst in the presence of Cs₂CO₃ (36%) and NaHCO₃ (38%) are found to be similar to that in the presence of Na₂CO₃ (34%). Similarly, with a better catalyst such as C3, the use of Cs₂CO₃ as the base resulted in improved % ee of 78.²⁵ With the same catalyst, the yield dropped from 58% with Cs₂CO₃ to just 14% in the absence of any base, even though ee remained good at 70%. All these experimental observations are in accordance with our mechanistic model and the enantiocontrolling transition states wherein the more important role of the base is identified in the turnover-

determining step that can enhance the yield but not the enantioselectivity. Hence, computational tools have been successfully employed toward enhancing the enantioselectivity in Heck–Matsuda arylation reaction. We believe a similar synergetic approach involving computations and in-line experiments could become beneficial to the emerging family of multicatalytic enantioselective transformations.²⁹

CONCLUSION

We have presented a comprehensive computational study on the mechanism of a dual-catalytic Heck–Matsuda arylation of cyclic alkenes by using aryl diazonium salts under a dual-catalytic condition involving Pd₂(dba)₃ and BINAM-derived chiral phosphoric acid. Among various mechanistic possibilities considered, the one with an explicit participation of sodium bicarbonate, which is generated in situ from the sodium carbonate base used in the reaction, has been found to be the most preferred pathway. In the precatalytic events, a favorable formation of a diazonium–phosphate ion pair, from the substrate aryl diazonium and the chiral phosphoric acid catalyst, is predicted as the most likely species to enter the catalytic cycle. The first catalytic step involving the oxidative addition of Pd(0) to the C_{aryl}–diazo bond, leading to a Pd–aryl intermediate, exhibits the highest barrier as compared to ensuing events such as migratory insertion and reductive elimination.

The critical step that dictates the enantioselectivity has been found to be the migratory insertion of the Pd–aryl to the bound cycloalkene. In the enantiocontrolling transition state, the sole chiral catalyst BDPA is dispositioned near the site of the reaction more like a counterion bound to sodium bicarbonate. The aryl migration to the *si* prochiral face of the cycloalkene has been found to be preferred over that to the *re* face, which leads to the experimentally observed enantiomer as the coupled product. A combination of weak noncovalent interactions between the catalysts and the substrates (such as C–H...O, C–H...N, C–H...F, C–H... π , lp... π , O–H... π , and C–F... π) in the enantiocontrolling transition state has been identified as responsible in rendering the *si*-face aryl migration energetically more preferred. A higher number of noncovalent interactions has been found to be effective toward enhanced enantioselectivities. Replacing the phenyl substituent of the N-aryl group in BDPA catalyst with an adamantyl group led to a higher number of noncovalent interactions and improved enantioselectivity for spirocyclic cyclopentene as the substrate. Additional computations on the migratory insertion transition states, with cycloheptene as the substrate, revealed that the noncovalent interactions between the catalyst and the substrate could favorably be modulated by changing the N-aryl group of BDPA by 3,5-diisopropoxyphenyl toward improved enantio-selectivity. The predicted enantioselectivities using our transition states have been found to be in very good agreement with that of the experimental observations, which could serve as a lead toward the design of catalyst libraries for asymmetric synthesis.

Computational Methods.

All calculations were carried out using the Gaussian09 suite of quantum chemical program.³⁰ Geometries of all stationary points were obtained using density functional theory (DFT) calculations with the B3LYP-D3³¹ functional in conjunction with basis set 6–31G** (C, H,

O, N, P, Na, and F) and LanL2DZ³² basis set consisting of an effective core potential (ECP) for 28 core electrons, and a double- ζ quality valence basis set for 18 valence electrons was used for palladium in the solvent phase. The effect of continuum solvation was incorporated by using the Truhlar–Cramer SMD solvation model,³³ wherein the full solute electron density is employed without defining partial atomic charges as well as a universal solvation model. Because the experimental studies employed toluene, MTBE (methyl *tert*-butyl ether), and toluene/MTBE (1:1) as the solvents, we have used the continuum dielectric of toluene ($\epsilon = 2.38$), MTBE ($\epsilon = 4.50$), and an average dielectric of toluene–MTBE ($\epsilon = 3.44$). Fully optimized geometries of all the stationary points were characterized by frequency calculations to verify that the TSs have one and only one imaginary frequency as desired for the given reaction coordinate, and all minimum energy structures have only positive Hessian index. The intrinsic reaction coordinate (IRC) calculations were performed at the B3LYP-D3 level of theory to further authenticate that the TS on the energy profiles connects to the respective minima on either side of the first-order saddle point. The enthalpy and Gibbs free energy in the solvent phase for all stationary points were obtained by adding the zero-point vibrational energy (ZPVE) and thermal energy corrections obtained by using standard statistical mechanics approximations at 298.15 K and 1 atm pressure. Thermal Gibbs free energy corrections were calculated based on the rigid rotor-harmonic oscillator (RRHO) approximation of Grimme.³⁴ Additional single-point energy refinements were done at the **M1**(mix) = SMD($\epsilon=3.44$)/M06/def2-TZVP, **M2**(tol) = SMD(toluene)/M06/def2-TZVP, **M3**(mix) = SMD($\epsilon=3.44$)/M06/6-31+G**,SDD-(Pd), **M4**(tol) = SMD(toluene)/ ω B97XD/def2-TZVP, and **M5**(tol) = SMD(toluene)/M06/6-311G**,SDD(Pd) and using SMD(toluene)/B3LYP-D3/6-31G**,LanL2DZ(Pd) optimized geometries.³⁵ The discussions in the manuscript are provided on the basis of the Gibbs free energies (kcal/mol) at the **M1** and **M2** levels of theory for spirocyclic cyclopentene derivatives and **M2** for cycloheptene derivatives in the main text.

Atoms in molecule (AIM) analyses were employed to identify important noncovalent interactions in the form of bond paths and bond critical points.³⁶ Electron densities at such bond critical points (ρ_{bcp}) are used in this study for evaluating the relative strength of the interactions. The Espinosa equation is employed to calculate the strength of noncovalent interactions (such as C–H...O, C–H...N, C–H...F, C–H... π , Ip... π , O–H... π , and C–F... π) by using topological parameters such as electron density as well as Laplacian at the bond critical points and kinetic energy density.³⁷ We have also carried out activation-strain analysis³⁸ on the important lower-energy diastereomeric TSs to understand the origin of the vital energy difference between the TSs. In the activation-strain model, the activation energy (E^\ddagger) is equated to the sum of distortions in the reactant geometries (E_{d}^\ddagger) as noted in the TS structures as compared to the respective ground-state geometries and the interaction energy (E_{int}^\ddagger) between such distorted fragments in the TS geometries. Therefore, the activation barrier is described as $E^\ddagger = E_{\text{d}}^\ddagger + E_{\text{int}}^\ddagger$. The energetic-span model developed by Shaik and Kozuch was applied to the computed catalytic cycles to evaluate the energetic span for various likely pathways considered in this study.³⁹

Supplementary Material

Refer to Web version on PubMed Central for supplementary material.

ACKNOWLEDGMENTS

Generous computing time from the SpaceTime supercomputing at IIT Bombay is acknowledged. Y.R. is grateful to IIT Bombay for providing a research associateship. C.-C.T. thanks Ministry of Science and Technology, Taiwan, for a postdoctoral fellowship (106-2917-1-564-056).

REFERENCES

- (1). (a)Chen D-F; Han Z-Y; Zhou X-L; Gong L-Z Asymmetric Organocatalysis Combined with Metal Catalysis: Concept, Proof of Concept, and Beyond. *Acc. Chem. Res* 2014, 47, 2365–2377. [PubMed: 24911184] (b)Parmar D; Sugiono E; Raja S; Rueping M Complete Field Guide to Asymmetric BINOL-Phosphate Derived Brønsted Acid and Metal Catalysis: History and Classification by Mode of Activation; Brønsted Acidity, Hydrogen Bonding, Ion Pairing, and Metal Phosphates. *Chem. Rev* 2014, 114, 9047–9153. [PubMed: 25203602] (c)Du Z; Shao Z Combining Transition Metal Catalysis and Organocatalysis – an Update. *Chem. Soc. Rev* 2013, 42, 1337–1378. [PubMed: 23154522] (d)Inamdar SM; Shinde VS; Patil NT Enantioselective Cooperative Catalysis. *Org. Biomol. Chem* 2015, 13, 8116–8162. [PubMed: 26123696] (e)Allen AE; MacMillan DWC Synergistic Catalysis: A Powerful Synthetic Strategy for New Reaction Development. *Chem. Sci* 2012, 3, 633–658.(f)Krautwald S; Carreira EM Stereodivergence in Asymmetric Catalysis. *J. Am. Chem. Soc* 2017, 139, 5627–5639. [PubMed: 28384402] (g)Dochain S; Vetica F; Puttreddy R; Rissanen K; Enders D Combining Organocatalysis and Lanthanide Catalysis: A Sequential One-Pot Quadruple Reaction Sequence/Hetero-Diels-Alder Asymmetric Synthesis of Functionalized Tricycles. *Angew. Chem., Int. Ed* 2016, 55, 16153–16155.(h)Singha S; Patra T; Daniliuc CG; Glorius F Highly Enantioselective [5 + 2] Annulations through Cooperative N-Heterocyclic Carbene (NHC) Organocatalysis and Palladium Catalysis. *J. Am. Chem. Soc* 2018, 140, 3551–3554. [PubMed: 29470082]
- (2). (a)Biffis A; Centomo P; Del Zotto A; Zecca M Pd Metal Catalysts for Cross-Couplings and Related Reactions in the 21st Century: A Critical Review. *Chem. Rev* 2018, 118, 2249–2295. [PubMed: 29460627] (b)Cherney AH; Kadunce NT; Reisman SE Enantioselective and Enantiospecific Transition-Metal-Catalyzed Cross-Coupling Reactions of Organometallic Reagents to Construct C–C Bonds. *Chem. Rev* 2015, 115, 9587–9652. [PubMed: 26268813]
- (3). (a)Oestreich M Breaking News on the Enantioselective Intermolecular Heck Reaction. *Angew. Chem., Int. Ed* 2014, 53, 2282–2285.(b)Kikukawa K; Matsuda T Reaction of Diazonium Salts with Transition Metals. I. Arylation of Olefins with Arenediazonium Salts Catalyzed by Zero Valent Palladium. *Chem. Lett* 1977, 6, 159–162.
- (4). (a)de Oliveira JM; Angnes RA; Khan IU; Polo EC; Heerdt G; Servilha BM; Menezes da Silva VH; Braga ACA; Correia CRD Enantioselective, Noncovalent, Substrate-Directable Heck–Matsuda and Oxidative Heck Arylations of Unactivated Five-Membered Carbocyclic Olefins. *Chem. - Eur. J* 2018, 24, 11738–11747. [PubMed: 29726052] (b)Li Z; Tong R Asymmetric Total Syntheses of (–)-Hedycoropyrans A and B. *J. Org. Chem* 2017, 82, 1127–1135. [PubMed: 28029045] (c)Oliveira CC; Pfaltz A; Correia CRD Quaternary Stereogenic Centers through Enantioselective Heck Arylation of Acyclic Olefins with Aryldiazonium Salts: Application in a Concise Synthesis of (R)-Verapamil. *Angew. Chem., Int. Ed* 2015, 54, 14036–14039.(d)Khan IU; Kattela S; Hassan A; Correia CRD Enantioselective total synthesis of the highly selective sphingosine-1-receptor VPC01091 by the Heck desymmetrization of a non-activated cyclopentene-fused spiro-pyrrolidinone. *Org. Biomol. Chem* 2016, 14, 9476–9480. [PubMed: 27722726] (e)Li Z; Ip FCF; Ip NY; Tong R Highly trans-Selective Arylation of Achmatowicz Rearrangement Products by Reductive γ -Deoxygenation and Heck–Matsuda Reaction: Asymmetric Total Synthesis of (–)-Musellarins A–C and Their Analogues. *Chem. - Eur. J* 2015, 21, 11152–11157. [PubMed: 26104266]
- (5). (a)Yasui S; Fujii M; Kawano C; Nishimura Y; Ohno A Dediazonation of Arenediazonium Salt with Trivalent Phosphorus Compounds by One-electron Transfer Mechanism. *Tetrahedron Lett* 1991, 32, 5601–5604.(b)Yasui S; Fujii M; Kawano C; Nishimura Y; Shioji K; Ohno A Mechanism of Dediazonation of Arenediazonium Salts with Triphenylphosphine and Trialkyl Phosphites. Generation of Cation Radicals from Trivalent Phosphorus Compounds and their Reactions. *J. Chem. Soc., Perkin Trans 2* 1994, 2, 177–183.

- (6). (a)Correia CRD; Oliveira CC; Salles AG Jr.; Santos EAF The First Examples of the Enantioselective Heck–Matsuda Reaction: Arylation of Unactivated Cyclic Olefins using Chiral Bisoxazolines. *Tetrahedron Lett* 2012, 53, 3325–3328. (b)Oliveira CC; Angnes RA; Correia CRD Intermolecular Enantioselective Heck–Matsuda Arylations of Acyclic Olefins: Application to the Synthesis of β -Aryl- γ -lactones and β -Aryl Aldehydes. *J. Org. Chem* 2013, 78, 4373–4385. [PubMed: 23570395] (c)deAzambuja F; Carmona RC; Chorro THD; Heerdt G; Correia CRD Noncovalent Substrate-Directed Enantioselective Heck Reactions: Synthesis of S- and P-Stereogenic Heterocycles. *Chem. - Eur. J* 2016, 22, 11205–11209. [PubMed: 27273079] (d)Kattela S; Heerdt G; Correia CRD Non-Covalent Carbonyl-Directed Heck–Matsuda Desymmetrizations: Synthesis of Cyclopentene-Fused Spirooxindoles, Spirolactones, and Spirolactams. *Adv. Synth. Catal* 2017, 359, 260–267. (e)Frota C; Polo EC; Esteves H; Correia CRD Regioselective and Stereoselective Heck–Matsuda Arylations of Trisubstituted Allylic Alkenols and their Silyl and Methyl Ether Derivatives to Access Two Contiguous Stereogenic Centers: Expanding the Redox-Relay Process and Application in the Total Synthesis of meso-Hexestrol. *J. Org. Chem* 2018, 83, 2198–2209. [PubMed: 29364666] (f)Silva AR; Polo EC; Martins NC; Correia CRD Enantioselective Oxy-Heck–Matsuda Arylations: Expedient Synthesis of Dihydrobenzofuran Systems and Total Synthesis of the Neolignan (–)-Conocarpan. *Adv. Synth. Catal* 2018, 360, 346–365. (g)Carmona RC; Köster OD; Correia CRD Chiral N,N Ligands Enabling Palladium-Catalyzed Enantioselective Intramolecular Heck–Matsuda Carbonylation Reactions by Sequential Migratory and CO Insertions. *Angew. Chem., Int. Ed* 2018, 57, 12067–12070.
- (7). (a)Werner EW; Mei T-S; Burckle AJ; Sigman MS Enantioselective Heck Arylations of Acyclic Alkenyl Alcohols using a Redox-Relay Strategy. *Science* 2012, 338, 1455–1458. [PubMed: 23239733] (b)Mei T-S; Patel HH; Sigman MS Enantioselective Construction of Remote Quaternary Stereocentres. *Nature* 2014, 508, 340–344. [PubMed: 24717439]
- (8). (a)Phipps RJ; Hamilton GL; Toste FD The Progression of Chiral Anions from Concepts to Applications in Asymmetric Catalysis. *Nat. Chem* 2012, 4, 603–614. [PubMed: 22824891] (b)Mahlau M; List B Asymmetric Counteranion-Directed Catalysis: Concept, Definition, and Applications. *Angew. Chem., Int. Ed* 2013, 52, 518–533. (c)Rauniyar V; Lackner AD; Hamilton GL; Toste FD Asymmetric Electrophilic Fluorination using an Anionic Chiral Phase-Transfer Catalyst. *Science* 2011, 334, 1681–1684. [PubMed: 22194571] (d)Brak K; Jacobsen EN Asymmetric Ion-Pairing Catalysis. *Angew. Chem., Int. Ed* 2013, 52, 534–561. (e)Hamilton GL; Kang EJ; Mba M; Toste FD A Powerful Chiral Counterion Strategy for Asymmetric Transition Metal Catalysis. *Science* 2007, 317, 496–499. [PubMed: 17656720] (f)Yamamoto E; Hilton MJ; Orlandi M; Saini V; Toste FD; Sigman MS Development and Analysis of a Pd(0)-Catalyzed Enantioselective 1,1-Diarylation of Acrylates Enabled by Chiral Anion Phase Transfer. *J. Am. Chem. Soc* 2016, 138, 15877–15880. [PubMed: 27960315] (g)Neel AJ; Milo A; Sigman MS; Toste FD Enantiodivergent Fluorination of Allylic Alcohols: Data Set Design Reveals Structural Interplay between Achiral Directing Group and Chiral Anion. *J. Am. Chem. Soc* 2016, 138, 3863–3875. [PubMed: 26967114] (h)Li F; Korenaga T; Nakanishi T; Kikuchi J; Terada M Chiral Phosphoric Acid Catalyzed Enantioselective Ring Expansion Reaction of 1,3-Dithiane Derivatives: Case Study of the Nature of Ion-Pairing Interaction. *J. Am. Chem. Soc* 2018, 140, 2629–2642. [PubMed: 29377689] (i)Tribedi S; Hadad CM; Sunoj RB Origin of Stereoselectivity in the Amination of Alcohols using Cooperative Asymmetric Dual Catalysis Involving Chiral Counterion. *Chem. Sci* 2018, 9, 6126–6133. [PubMed: 30090300] (j)Jindal G; Sunoj RB Mechanistic Insights on Cooperative Asymmetric Multi-Catalysis using Chiral Counterions. *J. Org. Chem* 2014, 79, 7600–7606. [PubMed: 25050786]
- (9). (a)Orlandi M; Hilton MJ; Yamamoto E; Toste FD; Sigman MS Mechanistic Investigations of the Pd(0)-Catalyzed Enantioselective 1,1-Diarylation of Benzyl Acrylates. *J. Am. Chem. Soc* 2017, 139, 12688–12695. [PubMed: 28800230] (b)Nelson HM; Williams BD; Miró J; Toste FD Enantioselective 1,1-Arylborylation of Alkenes: Merging Chiral Anion Phase Transfer with Pd Catalysis. *J. Am. Chem. Soc* 2015, 137, 3213–3216. [PubMed: 25723255] (c)Mukherjee S; List B Chiral Counteranions in Asymmetric Transition-Metal Catalysis: Highly Enantioselective Pd/Brønsted Acid-Catalyzed Direct α -Allylation of Aldehydes. *J. Am. Chem. Soc* 2007, 129, 11336–11337. [PubMed: 17715928] (d)Chai Z; Rainey TJ Pd(II)/Brønsted Acid Catalyzed Enantioselective Allylic C–H Activation for the Synthesis of Spirocyclic Rings. *J. Am. Chem. Soc* 2012, 134, 3615–3618. [PubMed: 22313246] (e)Jiang G; Halder R; Fang Y; List B A Highly

Enantioselective Overman Rearrangement through Asymmetric Counteranion-Directed Palladium Catalysis. *Angew. Chem., Int. Ed* 2011, 50, 9752–9755.(f)Banerjee D; Junge K; Beller M Cooperative Catalysis by Palladium and a Chiral Phosphoric Acid: Enantioselective Amination of Racemic Allylic Alcohols. *Angew. Chem., Int. Ed* 2014, 53, 13049–13053.(g)Tao Z-L; Zhang W-Q; Chen D-F; Adele A; Gong L-Z Pd-Catalyzed Asymmetric Allylic Alkylation of Pyrazol-5-ones with Allylic Alcohols: The Role of the Chiral Phosphoric Acid in C–O Bond Cleavage and Stereocontrol. *J. Am. Chem. Soc* 2013, 135, 9255–9258. [PubMed: 23734612] (h)Jiang T; Bartholomeyzik T; Mazuela J; Willersinn J; Bäckvall J-E Palladium(II)/Brønsted Acid-Catalyzed Enantioselective Oxidative Carbocyclization–Borylation of Enallenes. *Angew. Chem* 2015, 127, 6122–6125.(i)Smalley AP; Cuthbertson JD; Gaunt MJ Palladium-Catalyzed Enantioselective C–H Activation of Aliphatic Amines Using Chiral Anionic BINOL-Phosphoric Acid Ligands. *J. Am. Chem. Soc* 2017, 139, 1412–1415. [PubMed: 28064488] (j)Biswas S; Kubota K; Orlandi M; Turberg M; Miles DH; Sigman MS; Toste FD Enantioselective Synthesis of N,S-Acetals by an Oxidative Pummerer-Type Transformation using Phase-Transfer Catalysis. *Angew. Chem., Int. Ed* 2018, 57, 589–593.(k)Reid JP; Goodman JM Goldilocks Catalysts: Computational Insights into the Role of the 3, 3' Substituents on the Selectivity of BINOL-derived Phosphoric Acid Catalysts. *J. Am. Chem. Soc* 2016, 138, 7910–7917. [PubMed: 27227372] (l)Reid JP; Simon L; Goodman JM A Practical Guide for Predicting the Stereochemistry of Bifunctional Phosphoric Acid Catalyzed Reactions of Imines. *Acc. Chem. Res* 2016, 49, 1029–1041. [PubMed: 27128106] (m)Mori K; Isogai R; Kamei Y; Yamanaka M; Akiyama T Chiral Magnesium Bisphosphate-Catalyzed Asymmetric Double C(sp³)–H Bond Functionalization Based on Sequential Hydride Shift/Cyclization Process. *J. Am. Chem. Soc* 2018, 140, 6203–6207. [PubMed: 29741877]

- (10). (a)Nelson HM; Patel JS; Shunatona HP; Toste FD Enantioselective α -Amination Enabled by a BINAM-Derived Phase-Transfer Catalyst. *Chem. Sci* 2015, 6, 170–173. [PubMed: 25485073] (b)Hatano M; Ikeno T; Matsumura T; Torii S; Ishihara K Chiral Lithium Salts of Phosphoric Acids as Lewis Acid–Base Conjugate Catalysts for the Enantioselective Cyanosilylation of Ketones. *Adv. Synth. Catal* 2008, 350, 1776–1780.(c)Terada M; Sorimachi K; Uruguchi F Phosphorodiamidic Acid as a Novel Structural Motif of Brønsted Acid Catalysts for Direct Mannich Reaction of N-Acyl Imines with 1,3-Dicarbonyl Compounds. *Synlett* 2006, 1, 0133–0136.
- (11). Avila CM; Patel JS; Reddi Y; Saito M; Nelson HM; Shunatona HP; Sigman MS; Sunoj RB; Toste FD Enantioselective Heck–Matsuda Arylations through Chiral Anion Phase-Transfer of Aryl Diazonium Salts. *Angew. Chem., Int. Ed* 2017, 56, 5806–5811.
- (12). (a)Dang Y; Qu S; Wang Z-X; Wang X A Computational Mechanistic Study of an Unprecedented Heck-Type Relay Reaction: Insight into the Origins of Regio- and Enantioselectivities. *J. Am. Chem. Soc* 2014, 136, 986–998. [PubMed: 24380644] (b)Xu L; Hilton MJ; Zhang X; Norrby P-O; Wu Y-D; Sigman MS; Wiest O Mechanism, Reactivity, and Selectivity in Palladium-Catalyzed Redox-Relay Heck Arylations of Alkenyl Alcohols. *J. Am. Chem. Soc* 2014, 136, 1960–1967. [PubMed: 24410393] (c)de Oliveira Silva J; Angnes RA; Menezes da Silva VH; Servilha BM; Adeel M; Braga AAC; Aponick A; Correia CRD Intermolecular Noncovalent Hydroxy-Directed Enantioselective Heck Desymmetrization of Cyclopentenol: Computationally Driven Synthesis of Highly Functionalized cis-4-Arylcyclopentenol Scaffolds. *J. Org. Chem* 2016, 81, 2010–2018. [PubMed: 26836260]
- (13). These pathways differ primarily in terms of the mode of participation of the chiral phosphate in the catalytic cycle. More details on various pathways are provided in Schemes S3–S5, Figures S15–S17, and Tables S14–S16 in the Supporting Information. In path A (presented in the main manuscript), chiral phosphate is bound to NaHCO₃; when both the chiral phosphate and the bicarbonate (κ^1 binding) are directly bound to Pd, it is designated as path B. A κ^2 binding of the chiral phosphate as a ligand to Pd in the absence of NaHCO₃ is considered as path C, whereas in path D the chiral phosphate functions as a counterion and *dba* acts as a ligand.
- (14). (a) Details of base free counterion mode (path D) are provided in Scheme S3.(b) The energetic span calculations (Table S17) reveal that the span for path C is higher than that for path D in the absence of any base.
- (15). (a)Bucher D; Guidoni L; Carloni P; Rothlisberger U Coordination Numbers of K⁺ and Na⁺ Ions Inside the Selectivity Filter of the KcsA Potassium Channel: Insights from First Principles

- Molecular Dynamics. *Biophys. J* 2010, 98, L47–L49. [PubMed: 20483308] (b)Bankura A; Carnevale V; Klein ML Hydration Structure of Salt Solutions from *ab initio* Molecular Dynamics. *J. Chem. Phys* 2013, 138, 014501 ; full details of hydration of Na₂CO₃, NaHCO₃, and NaBF₄ are provided in the Supporting Information. [PubMed: 23298049]
- (16). Full details of IRC profile are provided in Figure S5 in the Supporting Information.
- (17). The geometry of the β -hydride elimination TS is provided in Figure S10 in the Supporting Information.
- (18). Full details of various conformers examined in the enantioselective migratory insertion step for catalyst C1 are provided in Figure S3 in the Supporting Information.
- (19). (a)Wheeler SE; Seguin TJ; Guan Y; Doney AC Noncovalent Interactions in Organocatalysis and the Prospect of Computational Catalyst Design. *Acc. Chem. Res* 2016, 49, 1061–1069. [PubMed: 27110641] (b)Sunoj RB Transition State Models for Understanding the Origin of Chiral Induction in Asymmetric Catalysis. *Acc. Chem. Res* 2016, 49, 1019–1028. [PubMed: 27101013] (c)Neel AJ; Hilton MJ; Sigman MS; Toste FD Exploiting Non-covalent π Interactions for Catalyst Design. *Nature* 2017, 543, 637–646. [PubMed: 28358089] (d)Reddi Y; Sunoj RB Mechanistic Studies on Stereoselective Organocatalytic Direct β -C–H Activation in an Aliphatic Chain by Chiral N-Heterocyclic Carbenes. *ACS Catal* 2015, 5, 1596–1603.(e)Knowles RR; Jacobsen EN Attractive Noncovalent Interactions in Asymmetric Catalysis: Links between Enzymes and Small Molecule Catalysts. *Proc. Natl. Acad. Sci. U. S. A* 2010, 107, 20678–20685. [PubMed: 20956302] (f)Wheeler SE; McNeil AJ; Muller P; Swager TM; Houk KN Probing Substituent Effects in Aryl–Aryl Interactions using Stereoselective Diels–Alder Cycloadditions. *J. Am. Chem. Soc* 2010, 132, 3304–3311. [PubMed: 20158182] (g)Li P; Maier JF; Vik EC; Yehl CJ; Dial BE; Rickher AE; Smith MD; Pellechia PJ; Shimizu KD Stabilizing Fluorine- π Interactions. *Angew. Chem., Int. Ed* 2017, 56, 7209–7212.(h)Coelho JAS; Matsumoto A; Orlandi M; Hilton MJ; Sigman MS; Toste FD Enantioselective Fluorination of Homoallylic Alcohols Enabled by the Tuning of Non-covalent Interactions. *Chem. Sci* 2018, 9, 7153–7158. [PubMed: 30310638] (i)Walden DMW; Ogba OM; Johnston RC; Cheong PH-Y Computational Insights into the Central Role of Nonbonding Interactions in Modern Covalent Organocatalysis. *Acc. Chem. Res* 2016, 49, 1279–1291. [PubMed: 27267964]
- (20). Milo A; Neel AJ; Toste FD; Sigman MS A Data-Intensive Approach to Mechanistic Elucidation Applied to Chiral Anion Catalysis. *Science* 2015, 347, 737–743. [PubMed: 25678656]
- (21). (a)Maji R; Champagne PA; Houk KN; Wheeler SE Activation Mode and Origin of Selectivity in Chiral Phosphoric Acid-Catalyzed Oxacycle Formation by Intramolecular Oxetane Desymmetrizations. *ACS Catal* 2017, 7, 7332–7339.(b)Ess DH; Houk KN Theory of 1,3-Dipolar Cycloadditions: Distortion/Interaction and Frontier Molecular Orbital Models. *J. Am. Chem. Soc* 2008, 130, 10187–10198. [PubMed: 18613669] (c)Bickelhaupt FM; Houk KN Analyzing Reaction Rates with the Distortion/Interaction-Activation Strain Model. *Angew. Chem., Int. Ed* 2017, 56, 10070–10086.(d)Duarte F; Paton RS Molecular Recognition in Asymmetric Counteranion Catalysis: Understanding Chiral Phosphate-Mediated Desymmetrization. *J. Am. Chem. Soc* 2017, 139, 8886–8896. [PubMed: 28582626]
- (22). For more details about the activation strain analysis, see Table S11 in the Supporting Information.
- (23). Different conformations and configurations and their energetics for diastereomeric TSs using C2 and C3 catalysts are provided in the Supporting Information. For full details, see Tables S4 and S6 in the Supporting Information.
- (24). Full details of interaction energies obtained through Espinosa equation are provided in Tables S3, S5, S7, and S8.
- (25). For more details about the experimental procedure and spectral and HPLC profiles, see part B of the Supporting Information.
- (26). It is noticed that the number of interactions between catalyst and substrates, as well as their strength, is found to be more in TS-*si*_h-C₄ than that in TS-*rec*_h-C₄. Full details are provided in Figures S11 and S12 in the Supporting Information.
- (27). Graphical summary of the strength of noncovalent interactions for cycloheptene system using catalysts C1, C2, C3, and C4 is provided in Figure S13.
- (28). The optimized geometries of the enantiocontrolling migratory insertion transition states (TS(2'–3)) for catalysts C3 in the presence of Na₂HPO₄ are provided in Figure S9.

- (29). (a)Sperger T; Sanhueza IA; Schoenebeck F Computation & Experiment – A Powerful Combination to Understand and Predict Reactivities. *Acc. Chem. Res* 2016, 49, 1311–1319. [PubMed: 27171796] (b)Peng Q; Duarte F; Paton RS Computing Organic Stereoselectivity-from Concepts to Quantitative Calculations and Predictions. *Chem. Soc. Rev* 2016, 45, 6093–6107. [PubMed: 27722685] (c)Houk KN; Cheong PH-Y Computational Prediction of Small-Molecule Catalysts. *Nature* 2008, 455, 309–313. [PubMed: 18800129]
- (30). Frisch MJ; Trucks GW; Schlegel HB; Scuseria GE; Robb MA; Cheeseman JR; Scalmani G; Barone V; Mennucci B; Petersson GA; Nakatsuji H; Caricato M; Li X; Hratchian HP; Izmaylov AF; Bloino J; Zheng G; Sonnenberg JL; Hada M; Ehara M; Toyota K; Fukuda R; Hasegawa J; Ishida N; Nakajima T; Honda Y; Kitao O; Nakai H; Vreven T; Montgomery JA Jr.; Peralta JE; Ogliaro F; Bearpark M; Heyd JJ; Brothers E; Kudin KN; Staroverov VN; Kobayashi R; Normand J; Raghavachari K; Rendell A; Burant JC; Iyengar SS; Tomasi J; Cossi M; Rega N; Millam MJ; Klene M; Knox JE; Cross JB; Bakken V; Adamo C; Jaramillo J; Gomperts R; Stratmann RE; Yazyev O; Austin AJ; Cammi R; Pomelli C; Ochterski JW; Martin RL; Morokuma K; Zakrzewski VG; Voth GA; Salvador P; Dannenberg JJ; Dapprich S; Daniels AD; Farkas Ö; Foresman JB; Ortiz JV; Cioslowski J; Fox DJ Gaussian09, Revision D.01; Gaussian, Inc.: Wallingford, CT, 2013.
- (31). Grimme S; Antony J; Ehrlich S; Krieg H A Consistent and Accurate *ab initio* Parametrization of Density Functional Dispersion Correction (DFT-D) for the 94 Elements H-Pu. *J. Chem. Phys* 2010, 132, 154104. [PubMed: 20423165]
- (32). Hay PJ; Wadt WR *Ab initio* Effective Core Potentials for Molecular Calculations. Potentials for K to Au Including the Outermost Core Orbitals. *J. Chem. Phys* 1985, 82, 299.
- (33). Marenich AV; Cramer CJ; Truhlar DG Universal Solvation Model Based on Solute Electron Density and on a Continuum Model of the Solvent Defined by the Bulk Dielectric Constant and Atomic Surface Tensions. *J. Phys. Chem. B* 2009, 113, 6378–6396. [PubMed: 19366259]
- (34). Grimme S Supramolecular Binding Thermodynamics by Dispersion-Corrected Density Functional Theory. *Chem. - Eur. J* 2012, 18, 9955. [PubMed: 22782805]
- (35). Full details of energetics evaluated at different levels of theory are provided in Tables S2, S4, S6, S9, and S10 in the Supporting Information.
- (36). (a)Buro fur Innovative Software; SBK-Software: Bielefeld, Germany, 2002.(b)Bader RFWA Quantum Theory of Molecular Structure and its Applications. *Chem. Rev* 1991, 91, 893–928. (c)Biegler-Konig F; Schonbohm J; Bayles D AIM2000. *J. Comput. Chem* 2001, 22, 545–559.
- (37). (a)Espinosa E; Molins E; Lecomte C Hydrogen Bond Strengths Revealed by Topological Analyses of Experimentally Observed Electron Densities. *Chem. Phys. Lett* 1998, 285, 170–173. (b)Espinosa E; Lecomte C; Molins E Experimental Electron Density Overlapping in Hydrogen Bonds: Topology vs. Energetics. *Chem. Phys. Lett* 1999, 300, 745–748.(c)Espinosa E; Souhassou M; Lachekar H; Lecomte C Topological Analysis of the Electron Density in Hydrogen Bonds. *Acta Crystallogr., Sect. B: Struct. Sci* 1999, 55, 563–572.
- (38). Bickelhaupt FM Understanding Reactivity with Kohn–Sham Molecular Orbital Theory: E2–SN2Mechanistic Spectrum and Other Concepts. *J. Comput. Chem* 1999, 20, 114–128.
- (39). (a)Kozuch S; Shaik S How to Conceptualize Catalytic Cycles? The Energetic Span Model. *Acc. Chem. Res* 2011, 44, 101–110. [PubMed: 21067215] (b)Kozuch S; Shaik S Kinetic-Quantum Chemical Model for Catalytic Cycles: The Haber–Bosch Process and the Effect of Reagent Concentration. *J. Phys. Chem. A* 2008, 112, 6032–6041. [PubMed: 18537227] (c)Kozuch S; Shaik S A Combined Kinetic–Quantum Mechanical Model for Assessment of Catalytic Cycles: Application to Cross-Coupling and Heck Reactions. *J. Am. Chem. Soc* 2006, 128, 3355–3365. [PubMed: 16522117] (d) Full details of energetic span model are provided in Supporting Information.

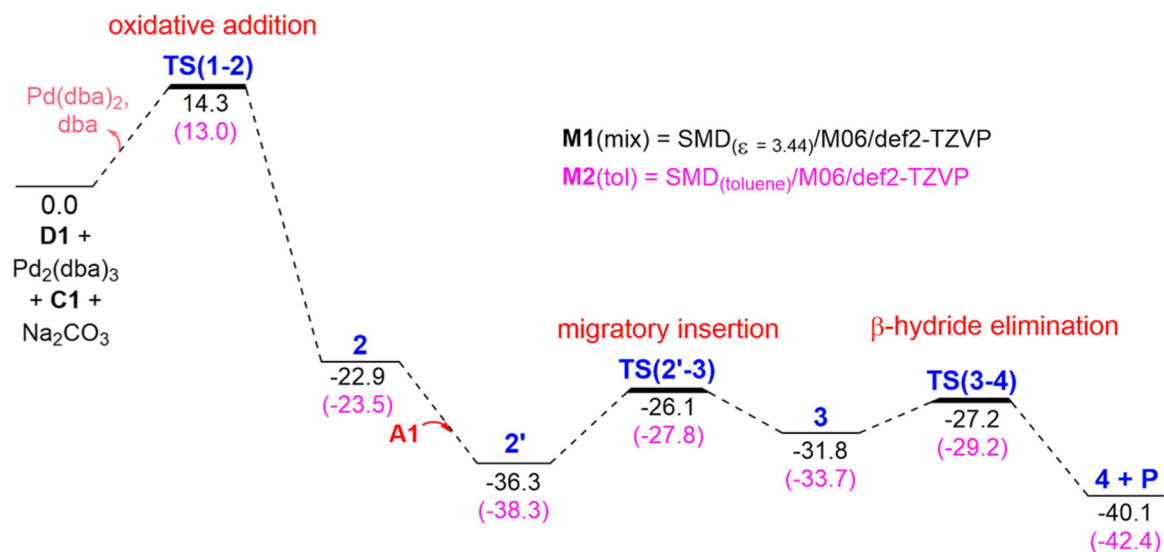


Figure 1. Gibbs free energy (kcal/mol) profile obtained using the geometries at the SMD_(toluene)/B3LYP-D3/6-31G**_{*,LanL2DZ(Pd)} level of theory for Heck–Matsuda arylation for spirocyclic cyclopentene derivative catalyzed by phosphoric acid **C1** and Pd(0). The free energies in parentheses are at **M1(mix)** and **M2(tol)** levels of theory. For the 1:1 mixed-solvent system of toluene and methyl *tert*-butyl ether (MTBE), an average dielectric constant of 3.44 is used.

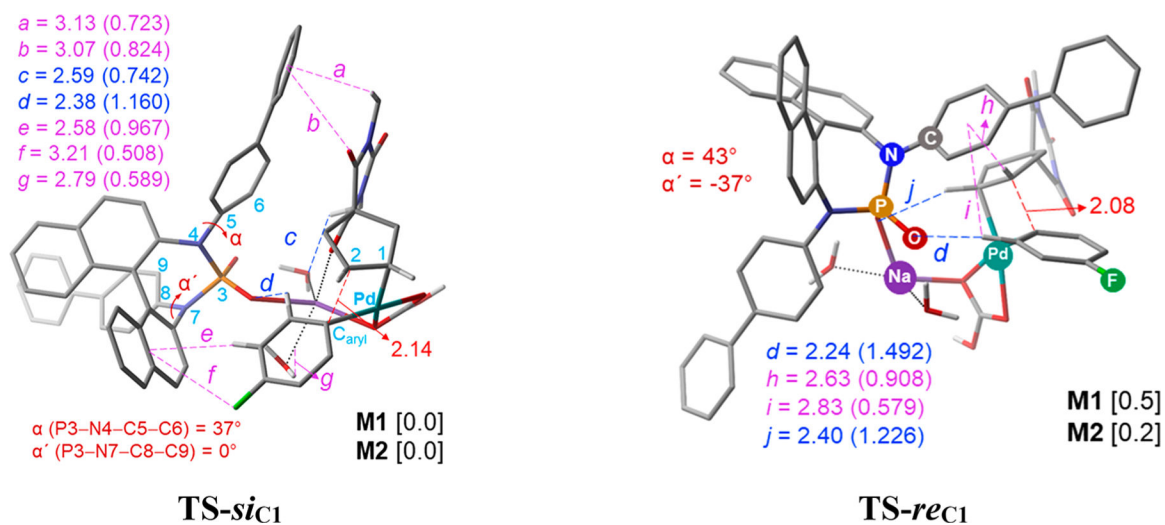


Figure 2. Optimized geometries of the enantiocontrolling migratory insertion transition states **TS(2'–3)** for catalyst **C1** obtained at the $\text{SMD}_{(\text{toluene})}/\text{B3LYP-D3/6-31G}^{**}, \text{LanL2DZ}(\text{Pd})$ level of theory. The relative free energies (kcal/mol) at **M1**(mix) and **M2**(tol) levels of theory are given in square brackets. The distances are in Å. The values in parentheses are electron densities at the bond critical points along the bond paths ($\rho \times 10^{-2}$ au).

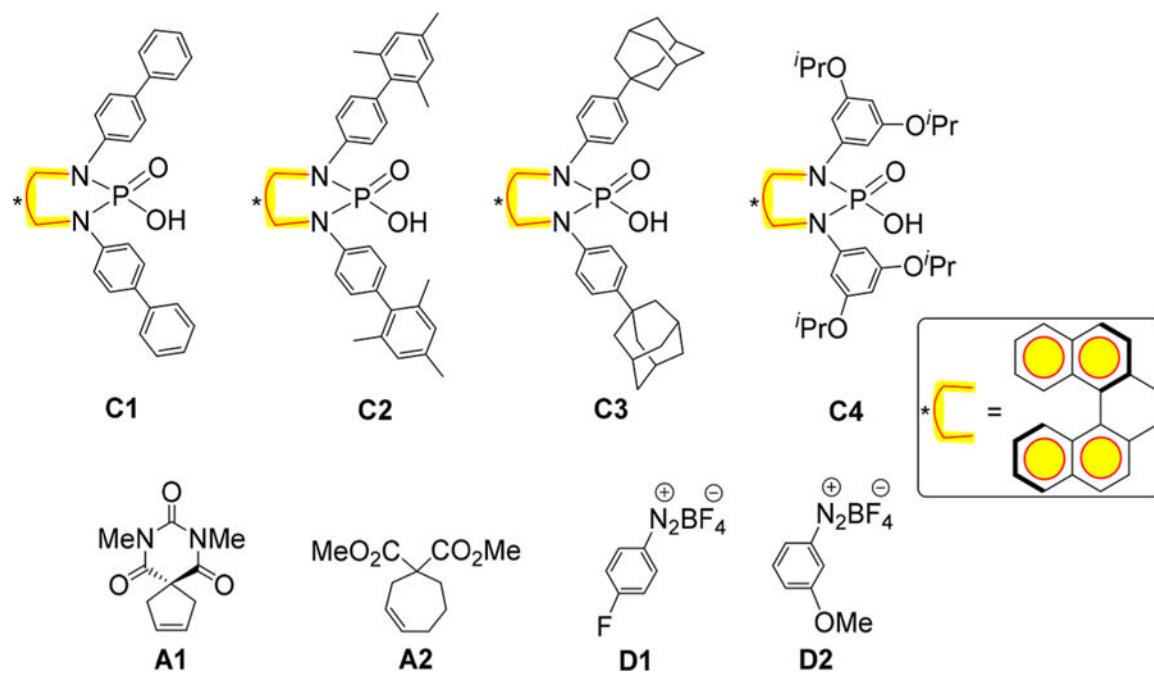


Figure 3. Modified catalysts and substrates considered for evaluating the role of noncovalent interactions in the enantiocontrolling migratory insertion transition state. Only a schematic representation of BINOL backbone is shown for all BDPA catalysts.

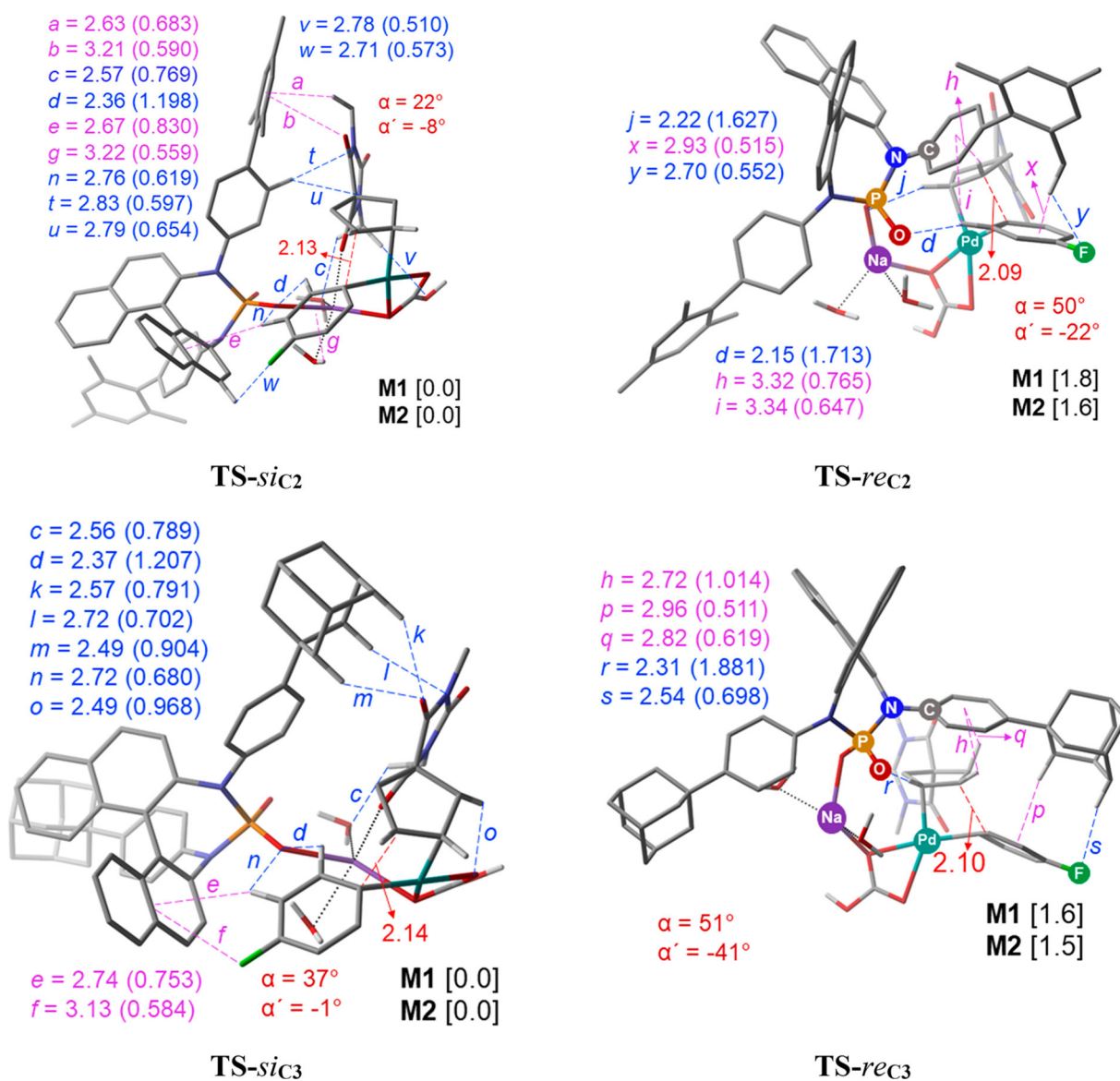


Figure 4. Optimized geometries of the enantiocontrolling migratory insertion transition states (TS(2'–3)) for catalysts **C2** and **C3** obtained at the SMD_(toluene)/B3LYP-D3/6–31G**,LanL2DZ(Pd) level of theory. The relative free energies (kcal/mol) at **M1**(mix) and **M2**(tol) levels of theory are given in square brackets. The distances are in Å. The values in parentheses are electron densities at the bond critical points along the bond paths ($\rho \times 10^{-2}$ au).

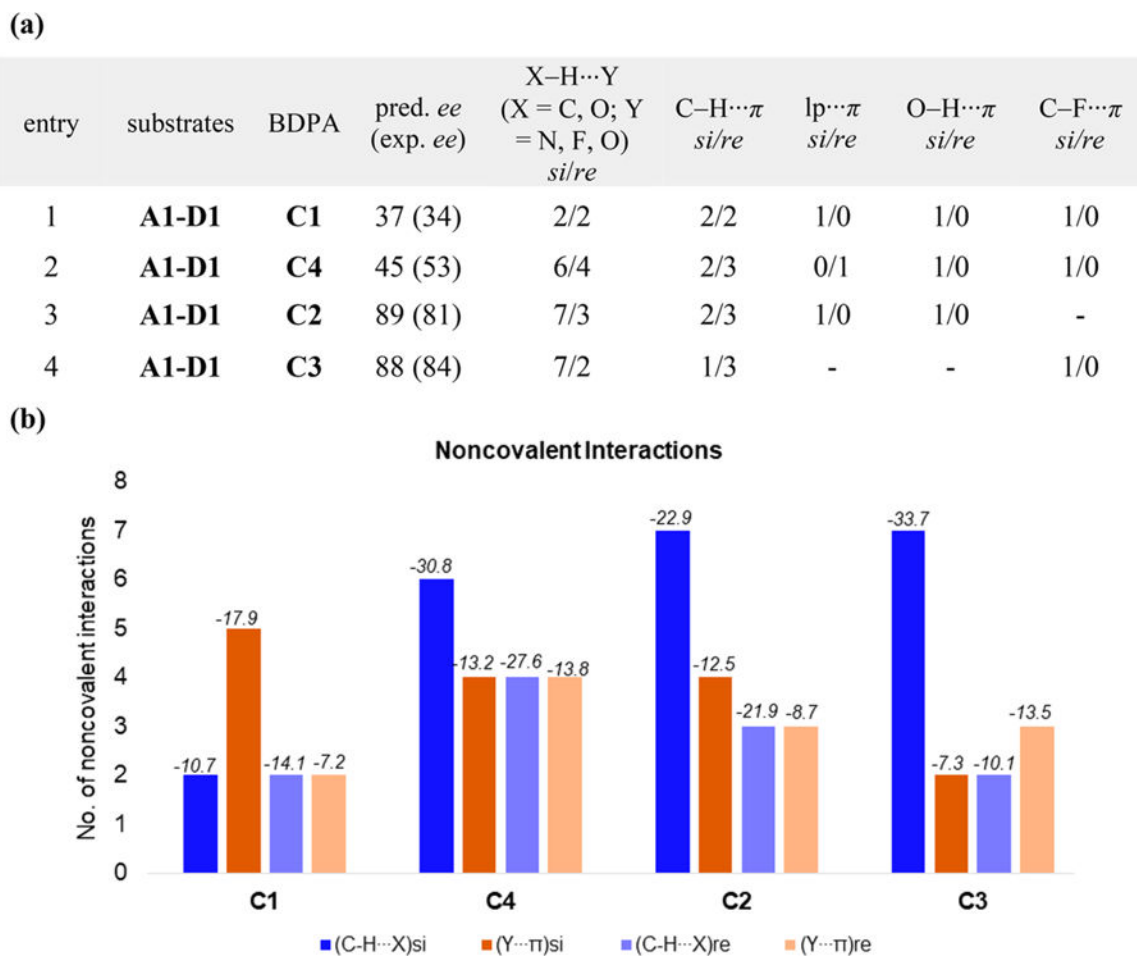


Figure 5. Graphical summary of important noncovalent interactions in the enantiocontrolling transition states for the Heck–Matsuda coupling between **A1** and **D1** substrates. Here, X = O, N, and F; Y = C–H, O–H, lp, and C–F. Values in italics given above the bar diagrams are the sum of the individual interaction energies computed using the electron densities at the respective bond critical points (ρ_{bcp}).

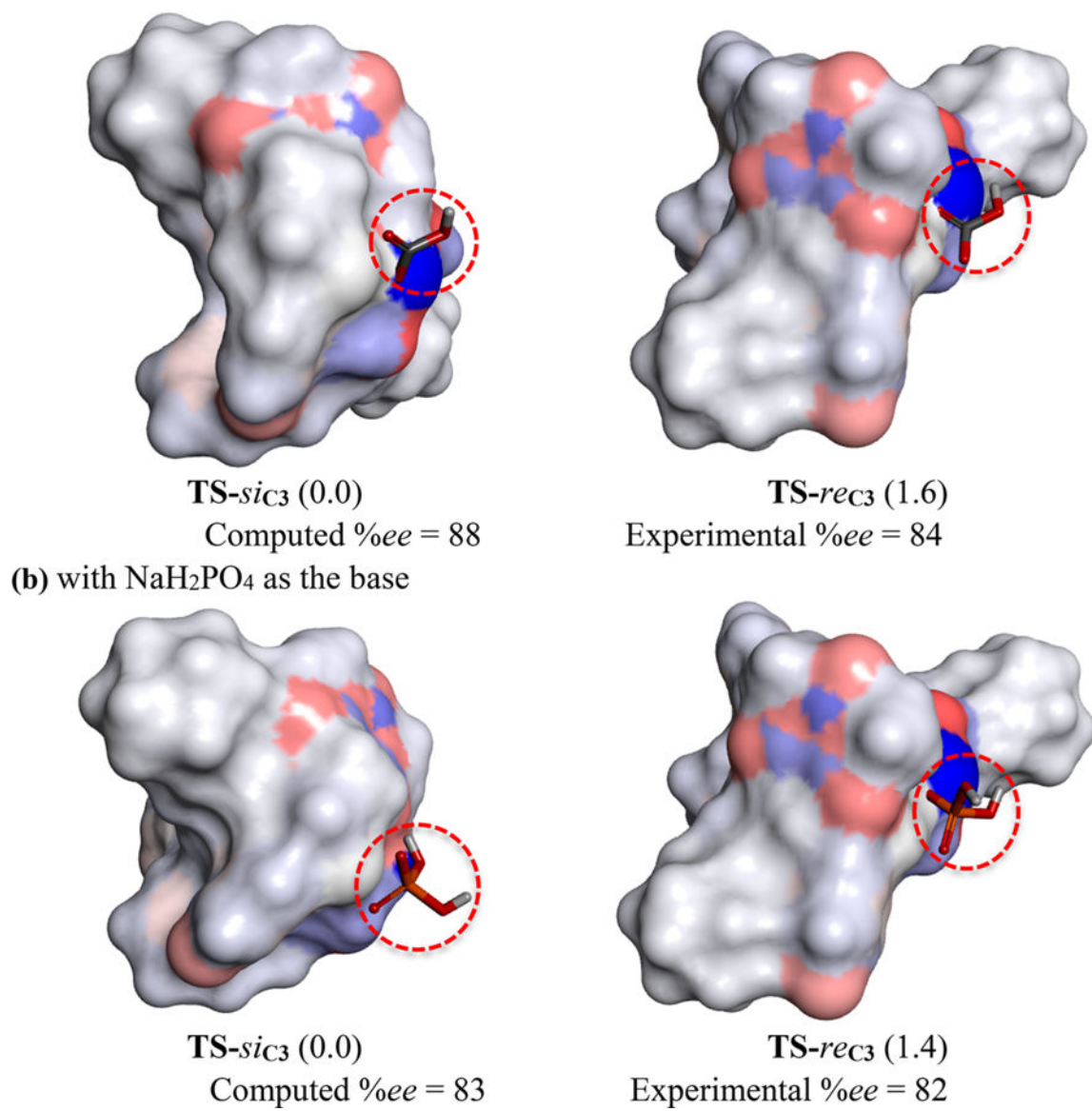
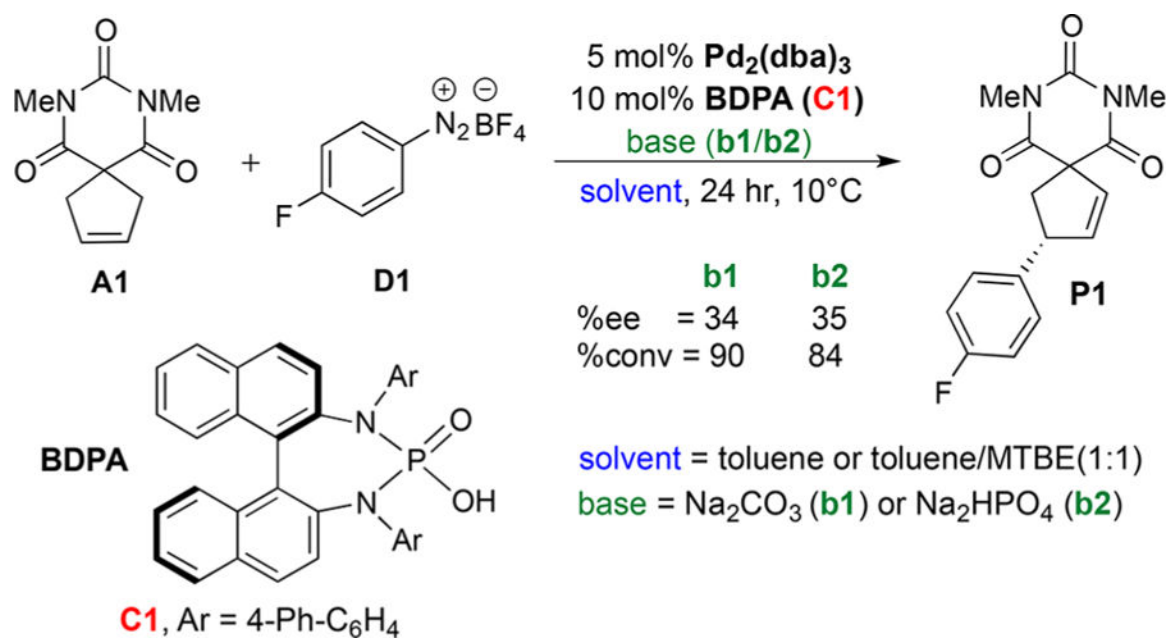
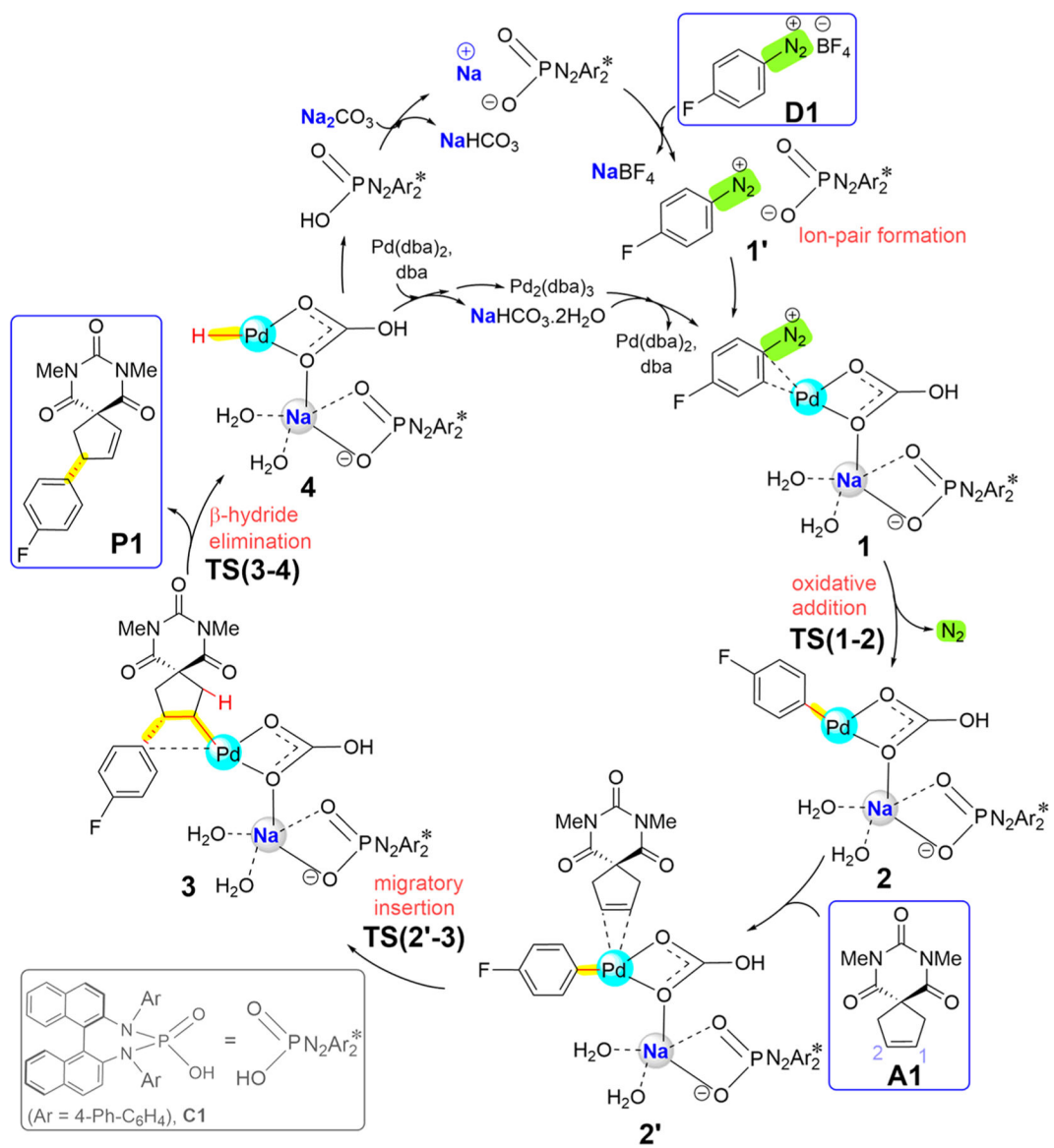


Figure 6. Space-filling models of enantiocontrolling migratory insertion transition states in the presence of (a) NaHCO₃ and (b) NaH₂PO₄ for **A1–D1** substrates with C3 catalyst. For better clarity, the position of the base is shown using a stick model inside the dotted circle.

**Scheme 1.**

Enantioselective Heck–Matsuda Arylation of a Spirocyclic Pentene under a Dual-Catalytic Condition Involving BINAM-Derived Phosphoric Acid (BDPA) and $\text{Pd}_2(\text{dba})_3$ (Where dba = trans,trans-Dibenzylideneacetone) Catalysts

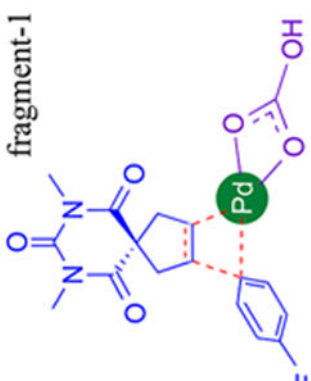
**Scheme 2.**

Key Steps Involved in the Enantioselective Heck–Matsuda Arylation of Spirocyclic Cyclopentene Using Chiral BDPA Catalyst **C1** in Conjunction with Pd₂(dba)₃ with Na₂CO₃ As the Base

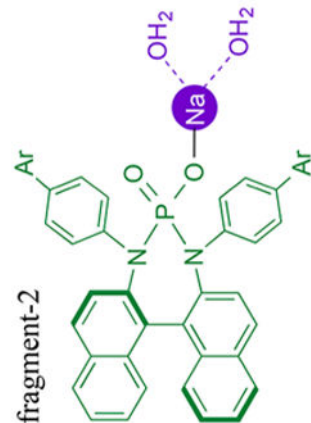
Table 1.

Distortion and Interaction Energies (kcal/mol) and Torsional Angles (deg) Along the Reaction Coordinate of the Enantiocontrolling Migratory Insertion Transition States for Various BDPA Catalysts and the Corresponding Fragments Using the Activation-Strain Analysis

Fragments used in Activation Strain Analysis												
BDPA catalyst	E_{int}^{\ddagger}			E_{dist}^{\ddagger}			ϕ (C _{aryl} -Pd-C1-C2)			α'		
	si	re	re	si	re	re	si	re	si	re	re	
C1	-53.83	-43.63	55.79	62.53	62.53	-18.8	12.3	43	0	-37		
C2	-54.11	-42.97	56.18	62.82	56.18	-18.2	17.6	50	-8	-22		
C3	-51.88	-46.57	57.06	60.46	57.06	-19.5	17.6	37	-1	-41		
C4	-58.72	-46.67	59.77	67.17	59.77	-19.5	11.9	47	-5	-38		



fragment-1



fragment-2

Table 2.

Comparison of Experimental and Computed ee's for Heck–Matsuda Arylation of Various Cyclic Olefins Catalyzed by a Combination of BDPAs and Pd₂(dba)₃

entry	cyclo alkene	aryl diazonium salt	BDPA	base	solvent	conv (%)	ee (exp)	ee (comp)
1	A1	D1	C1	none	toluene/MTBE (1/1)	7	36	25
2	A1	D1	C3	none	toluene/MTBE (1/1)	14	70	83
3	A1	D1	C1	b1	toluene/MTBE (1/1)	90	34	37
4	A1	D1	C4	b1	toluene/MTBE (1/1)	73	53	45
5	A1	D1	C2	b1	toluene/MTBE (1/1)	71	81	89
6	A1	D1	C3	b1	toluene/MTBE (1/1)	83	84	88
7	A2	D2	C1	b2	toluene	92 ^a	9	2
8	A2	D2	C2	b2	toluene	74 ^a	14	32
9	A2	D2	C3	b2	toluene	63	22	48

^a Isolated yields. **b1** = Na₂CO₃ and **b2** = Na₂HPO₄